



# Mechanical properties and growth mechanisms of long and small fatigue cracks in as-deposited bulk cold spray Al-6061



Christopher M. Sample <sup>a</sup>, Anthony G. Spangenberger <sup>a,\*</sup>, Victor K. Champagne <sup>b</sup>, Diana A. Lados <sup>a</sup>

<sup>a</sup> Worcester Polytechnic Institute, Integrative Materials Design Center, Worcester, MA, USA

<sup>b</sup> U.S. Army Research Laboratory, U.S. Army Combat Capabilities Development Command Weapons and Materials Research Directorate, Aberdeen, MD, USA

## ARTICLE INFO

### Keywords:

Cold spray  
Aluminum alloys  
Fatigue crack growth mechanisms  
Small fatigue cracks  
Interface strength

## ABSTRACT

Cold spray depositions are created by accelerating powder particles at a substrate at supersonic speeds to create a deposition with effective metallurgical and mechanical bonding. To progress from coatings/repairs to bulk additive depositions suitable for structural components, fatigue properties and microstructure-scale crack growth mechanisms must be established. In this study, the microstructure, tensile properties, and crack growth behavior were systematically investigated for as-sprayed Al-6061 and compared to those of wrought Al-6061-T6. Long fatigue crack growth behavior was investigated at two stress ratios ( $R = 0.1$  and  $0.7$ ) and two crack plane orientations with respect to the deposition direction. Small crack growth behavior was investigated at a stress ratio of  $R = 0.1$  in four crack plane orientations. Fractographic observations were made to identify the crack-microstructure interactions at different growth stages, and interparticle failure was determined to be the lifetime-limiting crack growth mechanism. A lap-shear testing method was developed to evaluate the interfacial shear strength of cold spray depositions at the interface with the substrate and to compare it to the strain energy release rates obtained from fatigue crack growth experiments. Design maps were created to relate loading conditions, crack orientation, and deposition ductility and predict the onset of interparticle growth.

## 1. Introduction and background

Cold Spray (CS) is a materials consolidation process whereby micron sized particles of a metal, ceramic and/or polymer are accelerated through a spray gun fitted with a de Laval rocket nozzle to form a coating or a near-net shaped part by means of ballistic impingement [1,2]. The feedstock powder particles are carried within a heated high-pressure gas (i.e., helium or nitrogen) such that they exit at supersonic velocities and consolidate upon impacting a suitable surface [1,2]. Originally starting as a coatings and repair technology, cold spray has grown into an additive manufacturing process.. The high kinetic energy of the process facilitates mechanical and metallurgical bonding to the substrate on which it is deposited [1,2,3]. Because the process is kept below the melting temperature of the powder, CS has many advantages over the traditional thermal spray method due to its solid-state nature. The particle-based deposition retains the microstructure of the atomized powder particles, and the kinetic energy imparted by impacting particles produces limited porosity and beneficial compressive residual stresses [1,2,4].

A comprehensive understanding of the effects of feedstock powder and

processing conditions on the resulting CS depositions and how these affect fatigue and fatigue crack growth (FCG) properties is needed to use CS materials for structurally critical components [5]. A survey of various materials studied in the literature generally shows that fatigue lives of CS-coated components are either reduced or maintained, although fatigue life improvements have been reported when a material with a higher fatigue life is deposited on a weaker material [6,7]. Fatigue cracks often initiate from voids within the deposition or defects at the interface between the deposition and substrate. Studies of bulk CS fatigue are comparatively limited in the literature, but generally show reduced fatigue lifetimes due to crack initiation at interlayer defects or poorly bonded powder particle boundaries [8–10]. Heat treatments can be applied to bulk depositions to improve fatigue life, however they are often undesirable in coating and repair applications due to their effects on the substrate [11].

Early-stage propagating cracks are typically categorized based on their size and mechanistic behavior as long or small. Long fatigue cracks (greater than ~1 mm in length and depth) are affected by closure and have lower effective driving force due to contact between the crack flanks [12]. In conventionally processed aluminum alloys, closure is often roughness-induced due to a crack's local deviations upon

\* Corresponding author.

E-mail address: [aspangenberger@wpi.edu](mailto:aspangenberger@wpi.edu) (A.G. Spangenberger).

interaction with characteristic microstructural features, including grain boundaries [13]. Small fatigue cracks, relative to the local microstructure or physical size of the crack, typically propagate faster than long cracks at the same nominal applied driving force and can be further classified as microstructurally small (making discrete interactions with microstructural features), physically small ( $a \leq 1$  mm), or short (small in one direction, typically depth), the latter two still being sufficiently small to not produce a wake that induces closure [14,15].

Limited crack growth data are found in the literature for CS materials [16,17]. Work by Gavras et al. [18] investigated long FCG of CS Al-6061 at various stress ratios ( $R = 0.1, 0.5$ , and  $0.7$ ) and in three heat treated conditions (as-sprayed, annealed, and T6). The crack growth mode was found to transition from transparticular to interparticular with increasing stress intensity, resulting in lower fracture toughness ( $\Delta K_{FT}$ ) compared to the wrought Al-6061-T6. Annealing heat treatment enhanced the bond strength between powder particles, increasing the material's ductility and resistance to crack growth. Small crack growth testing of CS Al-6061 was also conducted by Gavras et al. [19], where it was observed that the small FCG threshold ( $\Delta K_{th-app}$ ) of annealed CS Al-6061 was similar to the long crack threshold of the material due to the fine microstructure that produced only limited roughness-induced closure. Small crack data for coated, as-sprayed specimens was also presented, but due to the thickness of the coating, the crack only grew through  $30\ \mu\text{m}$  of CS and a true small FCG threshold was not obtained. Anisotropy in fracture toughness of bulk, as-sprayed CS Al-6061 depositions was studied by Julien et al. [20]. Fracture toughness of the CS material was found to be 40–50 % of that of wrought aluminum. Fracture toughness in the T-S/L-S orientation was found to be higher than in the L-T/T-L orientation ( $13.0\ \text{MPa}\sqrt{\text{m}}$  versus  $11.1\ \text{MPa}\sqrt{\text{m}}$ ), and the S-T/S-L had the lowest fracture toughness ( $10.8\ \text{MPa}\sqrt{\text{m}}$ ). Fracture surfaces that contained a greater area fraction of transparticular fracture were observed in orientations that had a higher fracture toughness.

Given the limited FCG data and understanding of processing-microstructure-property-performance relationships in the literature, the goal of this study is to expand on the understanding of the crack growth behavior of CS Al-6061 depositions to support design for structural applications. This is accomplished through systematic static (tension and shear) and dynamic (long and small FCG) testing to identify limiting microstructural damage phenomena and the role of crack orientation within the CS deposition. The novel shear test developed here provides a method to test bulk and interfacial specimens without the need for large depositions or adhesive-based techniques. From these observations, recommendations are made to improve processing parameters for enhanced static and cyclic properties, and design maps are created to provide heuristic engineering guidelines for structurally critical components.

## 2. Methodology

### 2.1. Materials and processing

Three separate CS depositions with similar processing conditions

**Table 1**

Cold spray deposition parameters for processing sets I, II, and III.

	Processing Set I	Processing Set II	Processing Set III
Powder Type	Al-6061	Al-6061	Al-6061
Powder Supply	Valimet Pre-processed	Valimet Pre-processed	Valimet, Heat Treated and Gas-Classified by Solvus Global
Powder Handling System	Humid air exposure prior to deposition VRC Gen 3	No humid air exposure VRC Gen 3	No humid air exposure VRC Gen 3
Process Gas	Helium 446 °C	Helium 446 °C	Helium 425 °C
Main Gas Temperature Set Point	3.792 MPa	3.792 MPa	3.447 MPa
Pressure Set Point	157 slm	157 slm	157 slm
Carrier Gas Flow Rate (actual)	2–2.5 RPM	2–2.5 RPM	3 RPM
Powder Feed RPM	Off	Off	Off
Powder Feeder Vibrator	400 mm/s	400 mm/s	400 mm/s
Robot Traverse Velocity	0.5 mm	0.5 mm	0.5 mm
Index Spacing			

were used in this study in as-sprayed conditions. Depositions will be referred to as processing sets I, II, and III, and their processing parameters are detailed in Table 1. For all three processing sets, a VRC Gen 3 system was used in the 21 kW configuration, having a PBI nozzle with a 2 mm diameter throat. A barrel-type applicator with a long pre-chamber was used. Substrates were cleaned with an abrasive pad and rinsed with alcohol to remove surface contaminants before spraying.

Valimet Al-6061 powder was used for all three depositions. The powder was heat treated before deposition to remove any water and hydroxide content at the surface, and subsequently rolled to break up any potential powder agglomerates that may have formed during heat treatment. The heat treatment was further designed to produce stable, overaged precipitates that provide the necessary ductility for particle deformation during deposition while maintaining moderate strength. Powder from processing set I was exposed to humid air between heat treatment and deposition to assess its impact on resulting deposition properties.

Completed CS depositions are shown in Fig. 1. Tensile bars were extracted from all three processing sets. Compact tension and lap shear specimens were extracted from processing set II, while surface flaw tension specimens were extracted from processing set III. Wrought specimens prepared for comparison were extracted from an Al-6061-T6 rolled plate.

### 2.2. Mechanical testing

Mechanical property tests were conducted using Instron servo-hydraulic systems equipped with precision force transducers having greater than  $\pm 0.25\ \text{kN}$  accuracy. All experiments were conducted at room temperature in laboratory air (relative humidity 20–40 %). Tensile testing was performed according to ASTM E8 [21] using a standard, subsize flat bar specimen, Fig. 2(a). Elongation was measured using a 3542 Epsilon extensometer.

Long FCG tests were conducted per ASTM E647 [12] at a frequency of 20 Hz and constant stress ratios of  $R = 0.1$  and  $0.7$ . Compact tension, C(T), specimens, Fig. 2(b), were used for the long FCG testing, using an initial notch with a length of 12.7 mm and a width of 0.252 mm introduced by wire-cut electrical discharge machining (EDM). Specimens are pre-cracked by 1 mm prior to data collection. Near-threshold crack growth and low Region II were established by the decreasing K method with a K-gradient of  $-220\ (\text{MPa}\sqrt{\text{m}})/\text{m}$ . Middle and upper Region II and Region III were acquired by the increasing K method with a K-gradient of  $220\ (\text{MPa}\sqrt{\text{m}})/\text{m}$ . To capture sufficient data points in Region III, the test was completed in constant load control at a reduced frequency of 5 Hz at crack growth rates above  $2.5 \cdot 10^{-4}\ \text{mm}/\text{cycle}$ . To calculate the effective, closure-corrected, stress intensity values ( $\Delta K_{eff}$ ), the adjusted compliance ratio (ACR) method was used [22]. The ACR method is a crack closure measurement technique that uses a front-face clip gage extensometer to calculate non-linearities in the load-displacement data associated with crack closure.

Small FCG data were produced using surface flaw tension, SF(T),

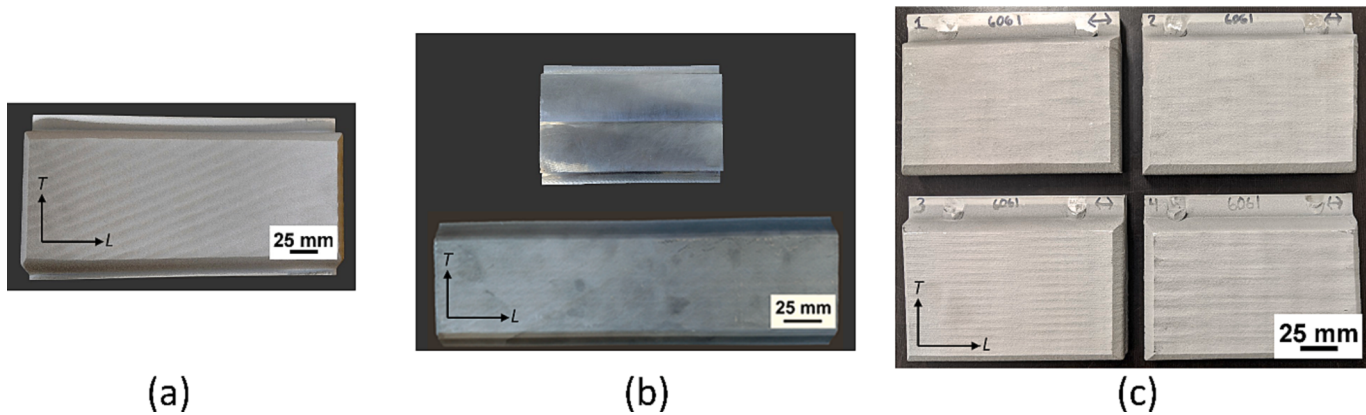


Fig. 1. As-sprayed CS Al-6061 depositions from processing sets (a) I, (b) II, and (c) III.

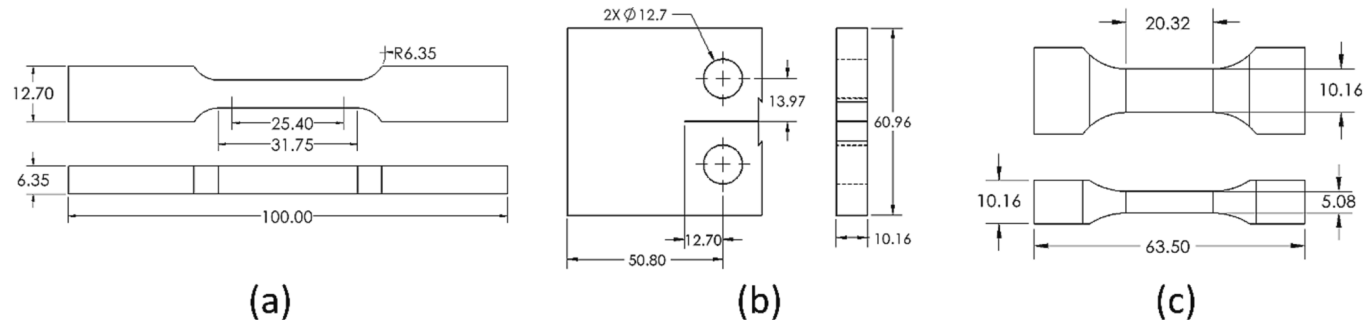


Fig. 2. Geometries of (a) tensile bar, (b) compact tension, and (c) surface flaw tension specimens. Units are in millimeters.

specimens shown in Fig. 2(c). Semi-circular surface flaw notches were introduced using a sinker EDM with an initial radial depth of 200  $\mu\text{m}$ . Direct current potential difference was used to measure the length of the small cracks. Two modes of small FCG test were conducted, K-control and constant load. The K-control tests were designed to establish small FCG thresholds by initiating cracks at  $5 \cdot 10^{-6} - 1 \cdot 10^{-5}$  mm/cycle and then applying a K-gradient of  $-1500$  (MPa $\sqrt{\text{m}}/\text{m}$ ) until cracks self-arrested at the threshold. Testing was then completed at an increasing K-gradient of  $1500$  (MPa $\sqrt{\text{m}}/\text{m}$ ) to overlap data in Region I and to complete Region II. The load-control small FCG tests were designed to study crack interaction with the microstructure. The load was increased step-wise in 220 N increments until crack growth was detected and then cracks were allowed to grow at constant load amplitude. Final crack growth rates for both test methods were calculated and reported using a combined seven-point polynomial/secant averaging method [23]. The long FCG tests were conducted with the crack growing in two orientations relative to the spray and deposition directions, as shown in Fig. 3

(a), and small crack growth was studied in four orientations indicated in Fig. 3(b).

### 2.3. Lap shear testing

Lap-shear testing was performed for CS Al-6061 depositions on wrought Al-6061-T6 substrates. A modified fixture was developed, based on ASTM D1002 [24], to constrain test coupons machined out of a larger deposition, Fig. 4. Lap-shear specimens have a length of 25.4 mm, a width of 6.4 mm, and a thickness of 4.7 mm. The area of material that is subjected to shear during testing ( $119.4 \text{ mm}^2$ ) matches the shear area of the triple lug shear test [25]. Lap-shear tests were conducted using an Instron servo-hydraulic test frame.

### 2.4. Metallographic specimen preparation and fractography

To prepare metallographic specimens for imaging, sectioning was

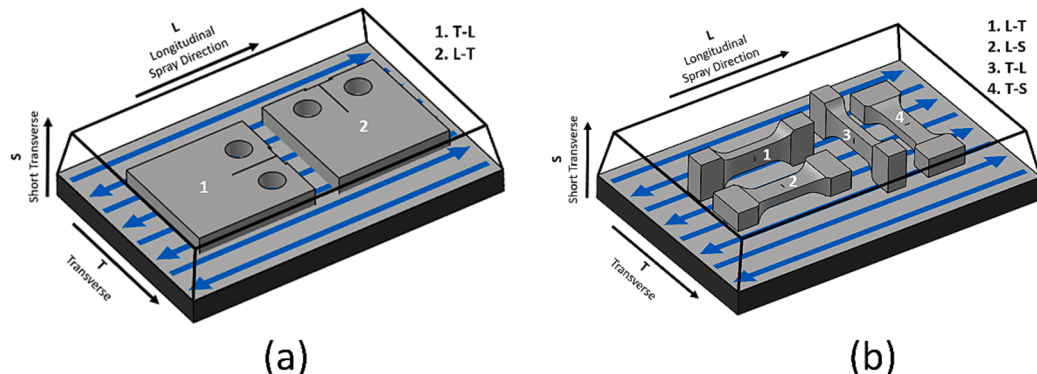
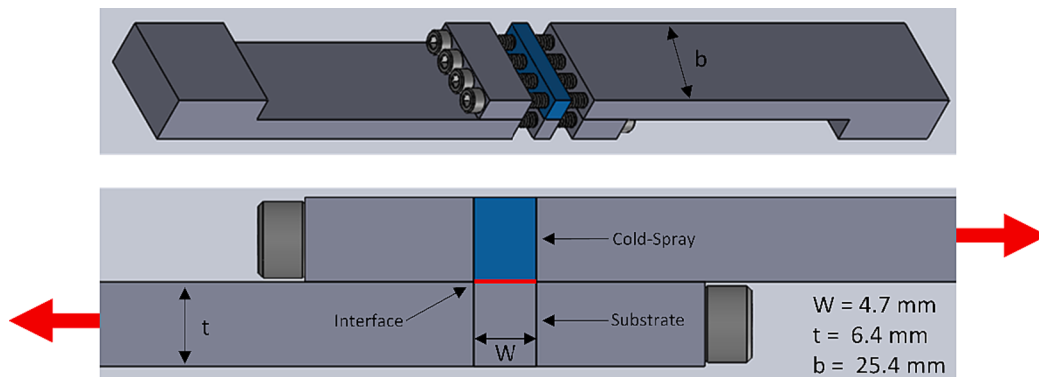


Fig. 3. Crack growth plane and direction for (a) long and (b) small cracks relative to the spray (L) and deposition (S) directions.



**Fig. 4.** Schematic view of the lap-shear test indicating the shear area.

first performed using an abrasive saw and/or EDM, followed by mounting in Bakelite. Specimens were polished with successively finer grit silicon carbide paper and diamond polish until a near-mirror surface was achieved. Final polishing was done in a vibratory polisher with colloidal silica. Etching of the CS Al-6061 specimens was performed by swabbing with Keller's reagent (95 % water, 2.5 % HNO<sub>3</sub>, 1.5 % HCl, 1.0 % HF) for 8–12 s, while etching of the wrought Al-6061 samples was done by electro-etching with Barkers reagent (24 % HBF<sub>4</sub>) at 35 V for 1–2 min. Fatigue specimens were sectioned on an abrasive saw after testing to expose the medial plane for side-profile imaging, and subsequently cleaned with acetone in an ultrasonic bath to remove debris. Microscopy studies were conducted using a Nikon MA 200 Eclipse optical microscope, equipped with the NIS-Elements D software for image analysis, and a JEOL-7000F field-emission scanning electron microscope (SEM). Specimens analyzed with electron backscatter diffraction (EBSD) were prepared in a Leica RES102 broad beam ion mill to minimize surface distortions from polishing and maximize diffraction pattern indexing rates.

### 3. Results and discussion

#### 3.1. Microstructure

The microstructures of the three processing sets of as-sprayed CS Al-6061 and wrought Al-6061-T6 are presented in Fig. 5. Across the three processing sets, the CS material had an average deposited particle size of 34.9 μm and an average grain size of 4.4 μm. The powder particle size and the average grain size were measured according to the ASTM E112 standard [26]. Powder particle boundaries are easily observed due to the contrast produced by etching of regions that experienced different plastic strain levels during deposition. There is slight anisotropy along the deposition direction due to the motion of the nozzle affecting impact velocity of powder particles. Powder particle boundaries in processing set I, Fig. 5(a), have greater contrast than in other processing sets, which

may be associated with lesser particle bonding. The wrought Al-6061-T6 had similar average grain sizes in the two planes along the rolling direction, 285 μm × 59 μm (L) and 219 μm × 64 μm (T).

An EBSD analysis was conducted on as-sprayed CS Al-6061 to characterize the structures within the powder particles, Fig. 6. Grain-like regions are apparent within individual powder particles and sub-grain/cellular structures with shared orientations can be observed within each of these grain-like regions. This crystallographic structure and naming convention are consistent with what has been reported in the literature [27,28]. Grains are more refined at particle boundaries than in the centers. Diffraction patterns cannot be indexed along particle boundaries due to the plastic deformation and resulting residual stress produced during deposition. The material was also studied in the annealed condition (344 °C for 8 h) to improve the band contrast and indexing rates, resulting in enhanced resolution at particle boundaries, Fig. 6(d-f).

#### 3.2. Tensile properties and fractography

The tensile properties of wrought Al-6061-T6 and as-sprayed CS Al-6061 from the three processing sets are shown in Table 2 along with representative stress-strain curves in Fig. 7. Statistical p-values are reported for a two-tailed Student's *t*-test assuming unequal variance. The CS material from processing set I exhibited the lowest ductility among the CS materials, with an elongation of 1.2 %. The low ductility was attributed to the exposure of powder particles to humid air prior to deposition, which inhibited metallurgical bonding through the development of oxide and hydroxide layers [29]. The surface oxides/hydroxides produce poor interparticle bonding that subsequently causes inferior material properties of the resultant cold sprayed material. Tensile properties of the deposition from processing set II, which had identical spray parameters to processing set I but were not exposed to humid air, showed greater ductility. Comparing orientations within set II, elongation is significantly higher in the longitudinal spraying direction as compared to the transverse direction ( $p = 0.011$ ), and no

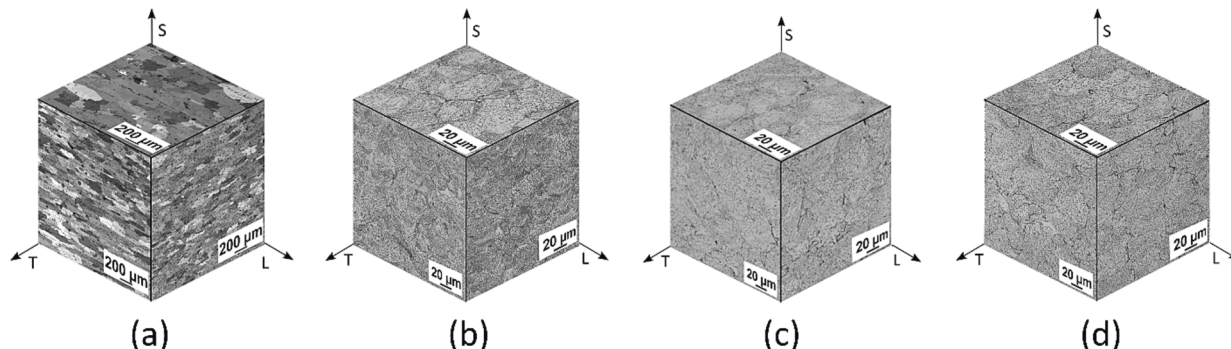


**Fig. 5.** Grain structures of (a) wrought Al-6061-T6 and (b, c, d) as-sprayed CS Al-6061 depositions from processing sets I, II, and III.

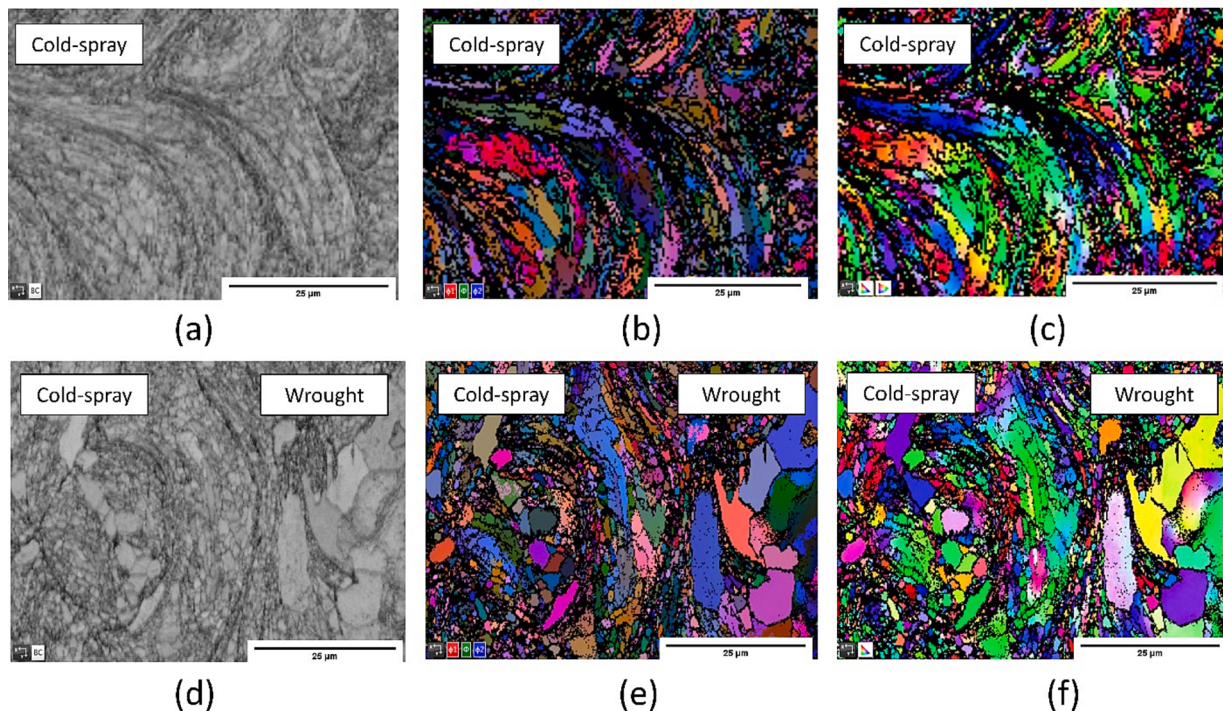


**Fig. 6.** ESDB of (a-c) as-sprayed CS Al-6061 and (d-f) annealed CS Al-6061 showing band contrast, IPF X, and Euler color, respectively.

**Table 2**

Tensile properties of wrought Al-6061-T6 and as-sprayed CS Al-6061 materials.

Material	Yield Strength (MPa)	Ultimate Tensile Strength (MPa)	E (GPa)	Elongation (%)
Wrought Al-6061-T6	291.6	317.1	70.3	17.0
As-sprayed CS Al-6061 L (I)	250.3	268.2	54.5	1.2
As-sprayed CS Al-6061 T (I)	251.2	271.3	55.3	1.0
As-sprayed CS Al-6061 L (II)	230.6	292.3	71.0	6.9
As-sprayed CS Al-6061 T (II)	231.0	289.6	70.3	5.7
As-sprayed CS Al-6061 L (III)	249.5	289.6	67.5	3.9

differences in tensile and yield strengths are observed ( $p = 0.616$ ). Sets II and III had an ultimate tensile strength of approximately 290 MPa, 8.5 % less than the wrought Al-6061-T6 material, and the differences between sets were not significant ( $p = 0.392$ ). However, significant differences in yield strength ( $p = 0.002$ ) and elongation ( $p < 0.001$ ) were observed between sets II and III, and conditions with greater yield strength had lower elongation. It is noteworthy that the gas temperature and pressure were slightly lower in processing set III, which may be responsible for the lesser mechanical property values.

Fractographic SEM images of the tensile samples from the low and high ductility depositions (processing sets I and II) are presented in Fig. 8. In samples with powders exposed to humid air and exhibiting low ductility (set I), powder particles are not well bonded together, producing a greater area fraction of un-bonded powder particle surfaces, Fig. 8(a). For specimens using powders without exposure to humid air with high ductility (set II), powder particle surfaces are still visible where incomplete bonding took place, however, there are large areas of ductile dimpling along powder particle boundaries, Fig. 8(b), which are

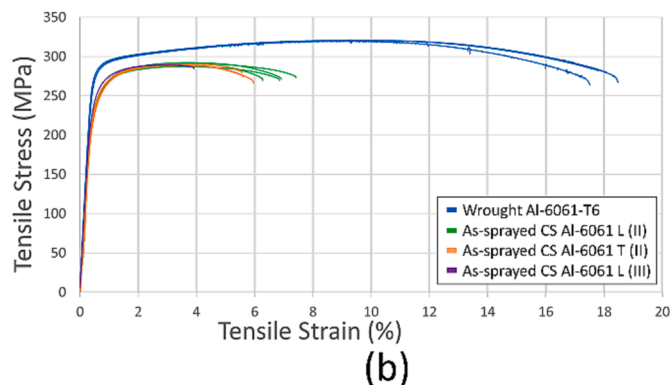
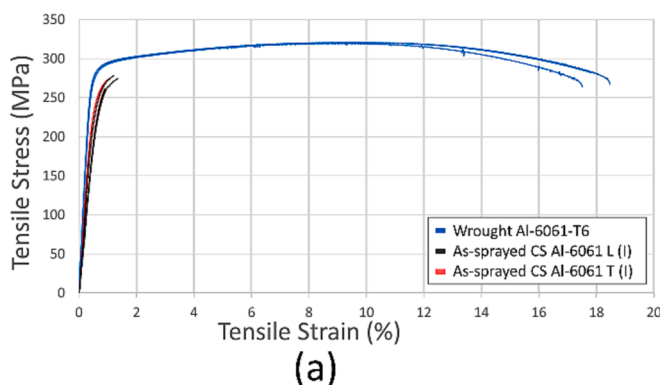


**Fig. 7.** Examples of tensile stress–strain curves for wrought Al-6061-T6 and as-sprayed CS Al-6061 prepared from (a) processing set I and (b) processing sets II and III.

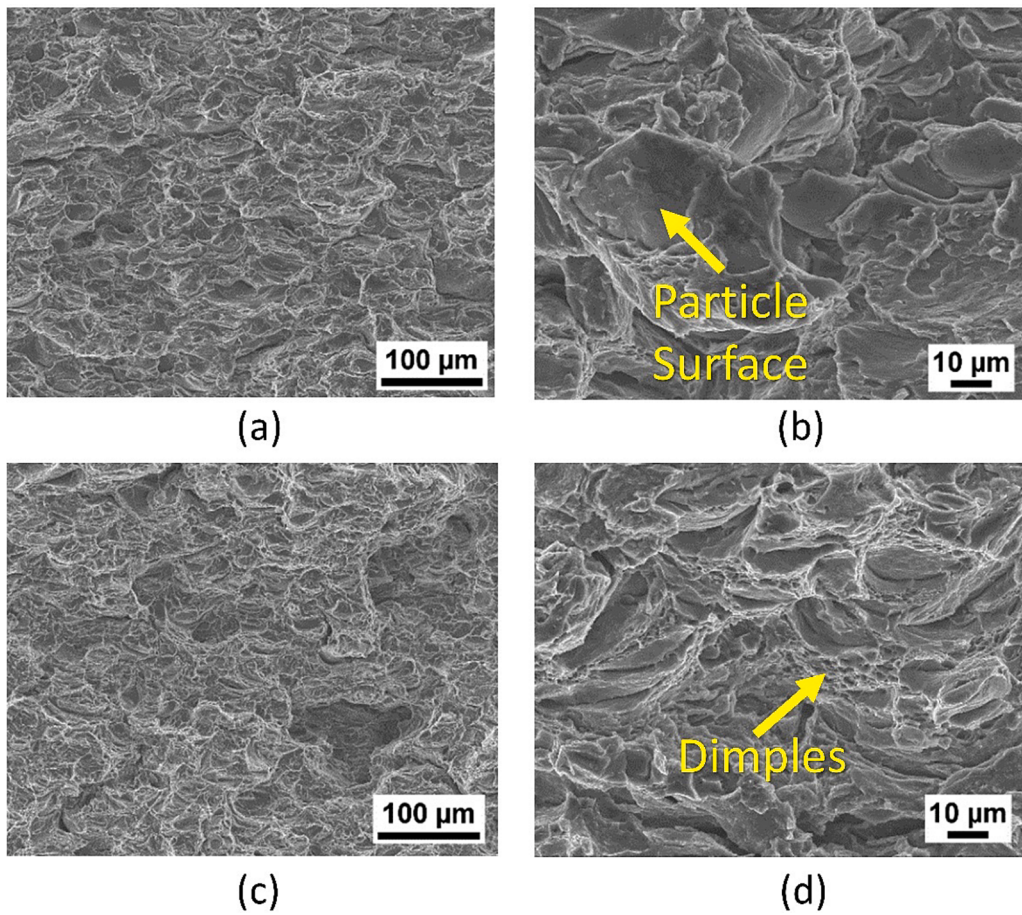


**Fig. 8.** SEM images – overviews and high magnifications – for tensile fracture surfaces of as-sprayed CS Al-6061 from (a,b) processing set I (air exposure, low ductility) and (c,d) processing set II (no air exposure, high ductility).

not present in the lower ductility deposition. The increase in particle bonding leads to an increase in the deposition's ductility, however, the persistence of incomplete bonding decreases the total ductility of the CS material as compared to the wrought aluminum.

### 3.3. Long fatigue crack growth data and mechanisms

Long FCG data at stress ratios of  $R = 0.1$  and  $0.7$  for both wrought Al-6061-T6 and as-sprayed CS Al-6061 are summarized in Table 3, with all FCG curves compared in Fig. 9. At stress ratio  $R = 0.1$ , the as-sprayed material had no discernable differences between crack growth rates in the two crack growth directions along and across the spray tracks (T-L and L-T), Fig. 9(a). The CS material has a slightly lower threshold than the wrought material,  $\Delta K_{\text{th-app}} = 2.3 \text{ MPa}\sqrt{\text{m}}$  as compared to  $\Delta K_{\text{th-app}} = 2.6 \text{ MPa}\sqrt{\text{m}}$ . Throughout Region II, crack growth of the CS material is identical to the wrought material before crack growth rates accelerate around  $\Delta K_{\text{app}} = 7.8 \text{ MPa}\sqrt{\text{m}}$  ( $K_{\text{max}} = 8.6 \text{ MPa}\sqrt{\text{m}}$ ). At  $R = 0.7$ , crack

growth curves shift toward lower  $\Delta K$  values due to mean stress effects, Fig. 9(b). The threshold for crack growth is more similar between the CS and wrought materials at higher stress ratio,  $\Delta K_{\text{th-app}} = 1.4 \text{ MPa}\sqrt{\text{m}}$  as compared to  $\Delta K_{\text{th-app}} = 1.5 \text{ MPa}\sqrt{\text{m}}$ . Crack growth rates are similar to the wrought material in low Region II, but the accelerated crack growth occurs at a much lower  $\Delta K_{\text{app}}$ , but at a similar  $K_{\text{max}} = 8.8 \text{ MPa}\sqrt{\text{m}}$ .

Crack growth mechanisms of the wrought Al-6061-T6 at  $R = 0.1$ , as observed by SEM fractographic analysis, are shown in Fig. 10. In Region I, the fracture surface is faceted due to transgranular growth. In Regions II and III, crack propagation is still transgranular, but with cleavage-like features and fatigue striations evident on the fracture surface until failure. Similar fractographic analyses were conducted for CS Al-6061 at  $R = 0.1$  in both crack orientations and are shown in Figs. 11 and 12. At low stress intensities, crack growth is transparticular and insensitive to particle boundaries in both orientations. Crack growth is not completely transgranular, as interactions with grains within powder particles are observed. As the stress intensity increases, there is a transition to a

**Table 3**

Summary of FCG thresholds ( $\Delta K_{\text{th-app}}$  and  $\Delta K_{\text{th-eff}}$ ), fracture toughness  $\Delta K_{\text{FT}}$ , and Paris Law constants (C and m) for all long crack growth testing conditions (processing set II). The  $\Delta K_{\text{th-eff}}$  values are calculated using the ACR method [22].

Material	Test Specimen	R	Orientation	$\Delta K_{\text{th-app}}$ [MPa $\sqrt{\text{m}}$ ]	$\Delta K_{\text{th-eff}}$ [MPa $\sqrt{\text{m}}$ ]	$\Delta K_{\text{FT}}$ [MPa $\sqrt{\text{m}}$ ]	C	m
Wrought Al-6061-T6			T-L	2.6	1.9	33.3	$6.3 \cdot 10^{-9}$	4.4
As-sprayed CS Al-6061		0.1	T-L	2.3	1.1	12.1	$3.0 \cdot 10^{-8}$	3.3
As-sprayed CS Al-6061	C(T)		L-T	2.2	1.3	12.0	$2.7 \cdot 10^{-8}$	3.6
Wrought Al-6061-T6			T-L	1.5	1.3	13.7	$2.3 \cdot 10^{-7}$	2.7
As-sprayed CS Al-6061		0.7	T-L	1.4	1.1	4.2	$3.8 \cdot 10^{-8}$	4.8
As-sprayed CS Al-6061			L-T	1.3	1.1	4.3	$8.8 \cdot 10^{-8}$	3.9

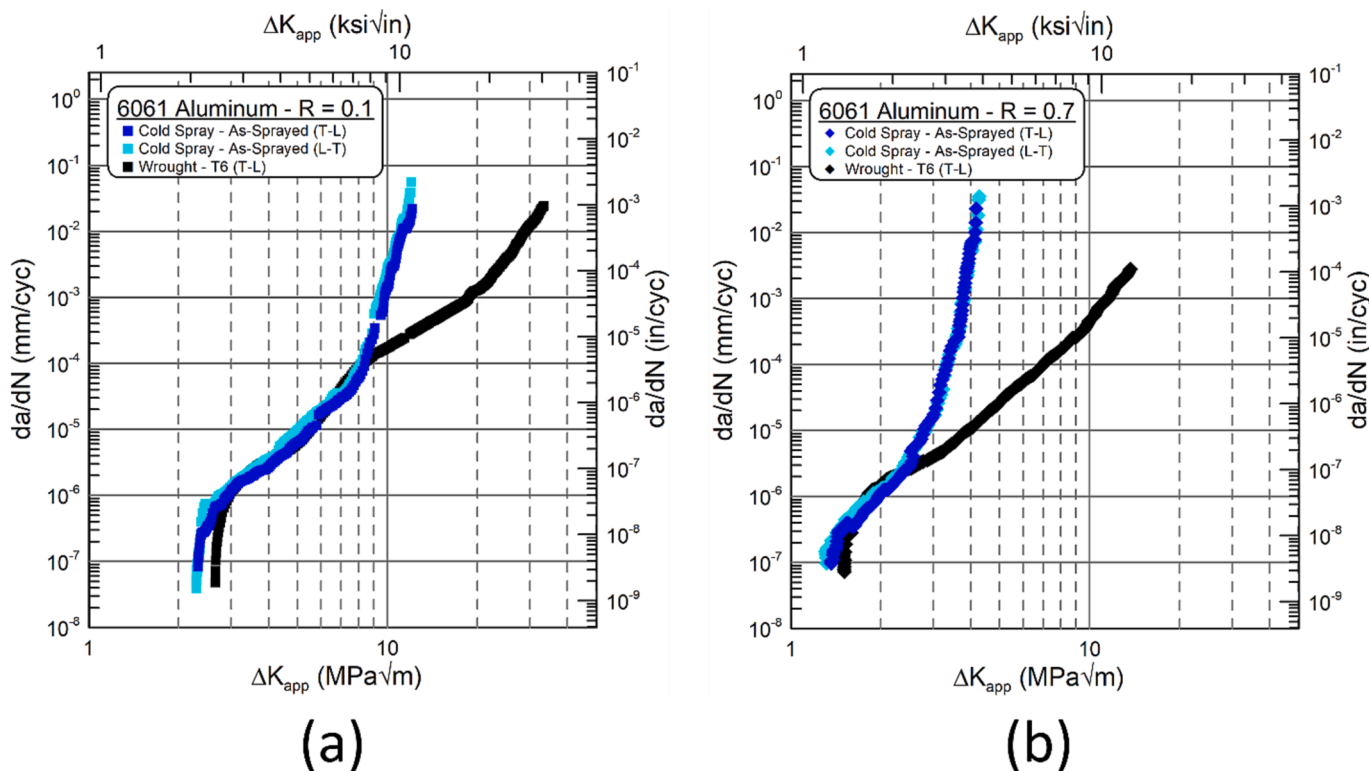


**Fig. 9.** Long FCG curves for wrought Al-6061-T6 and as-sprayed CS Al-6061 at (a)  $R = 0.1$  and (b)  $R = 0.7$ .

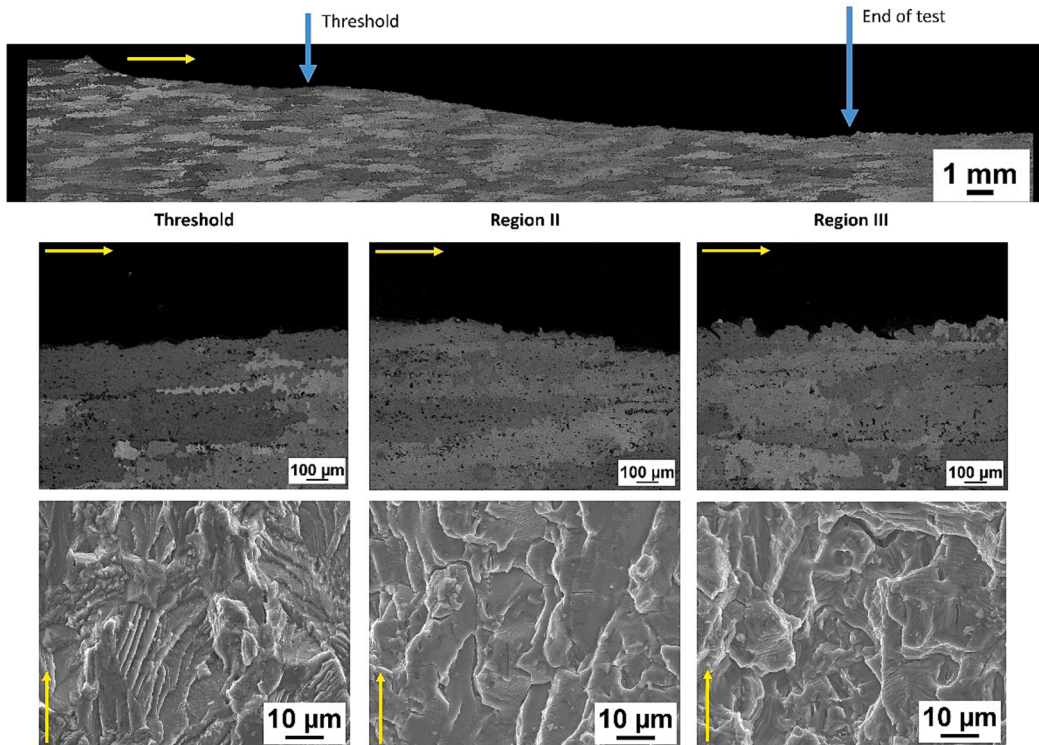


**Fig. 10.** Optical images (panoramic and high-magnification side profiles) and SEM fractography (top view) for wrought Al-6061-T6 at  $R = 0.1$  (C(T) specimen, T-L). Yellow arrows indicate crack growth direction.

mixed-mode transparticular and interparticular growth, where the crack interacts with particle boundaries that are not fully bonded. This mixed-mode transition begins at  $\Delta K_{app} = 3.4 \text{ MPa}\sqrt{\text{m}}$ , where the cyclic plastic zone is similar in size to a powder particle (cyclic plastic zone size  $r_y =$

$35 \mu\text{m}$ ). Interparticular (and in general, intergranular) crack growth is a static growth mechanism that is controlled by  $K_{max}$ . At  $K_{max} = 8.6 \text{ MPa}\sqrt{\text{m}}$ , crack growth becomes completely interparticular at crack lengths corresponding to the sharp increase in crack growth rates at the

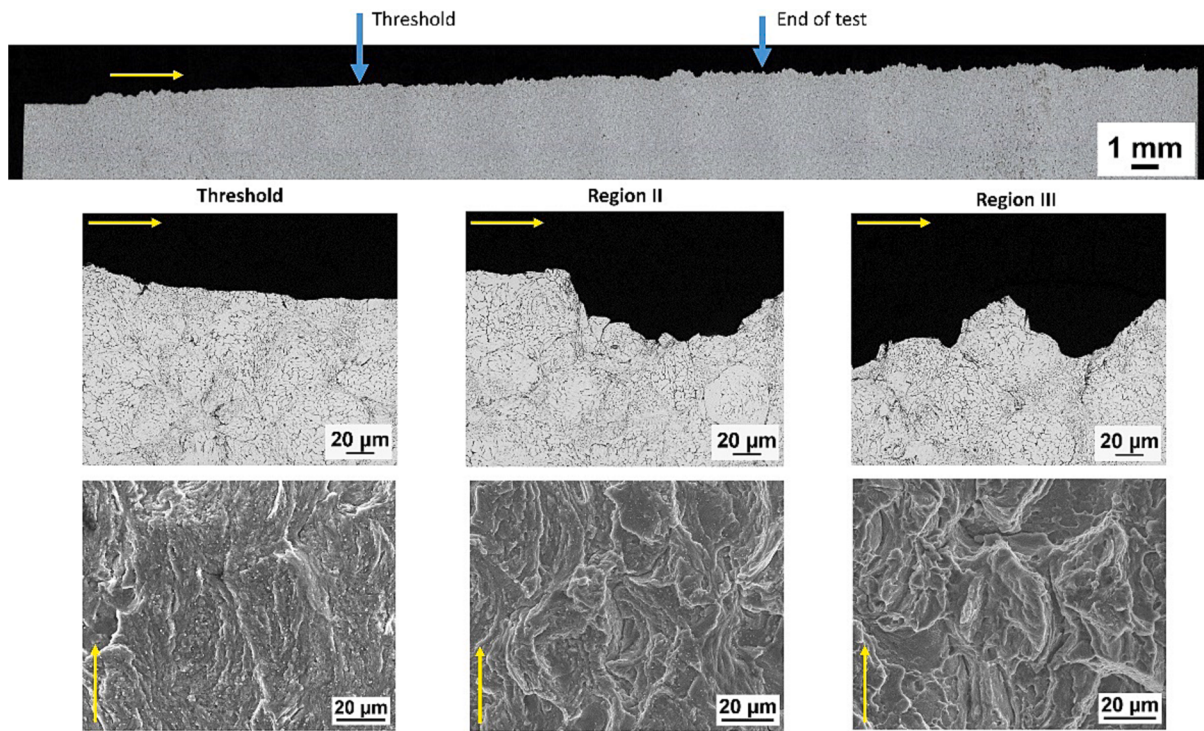


**Fig. 11.** Optical images (panoramic and high-magnification side profiles) and SEM fractography (top view) for as-sprayed CS Al-6061 at  $R = 0.1$  (C(T) specimen, T-L). Yellow arrows indicate crack growth direction.

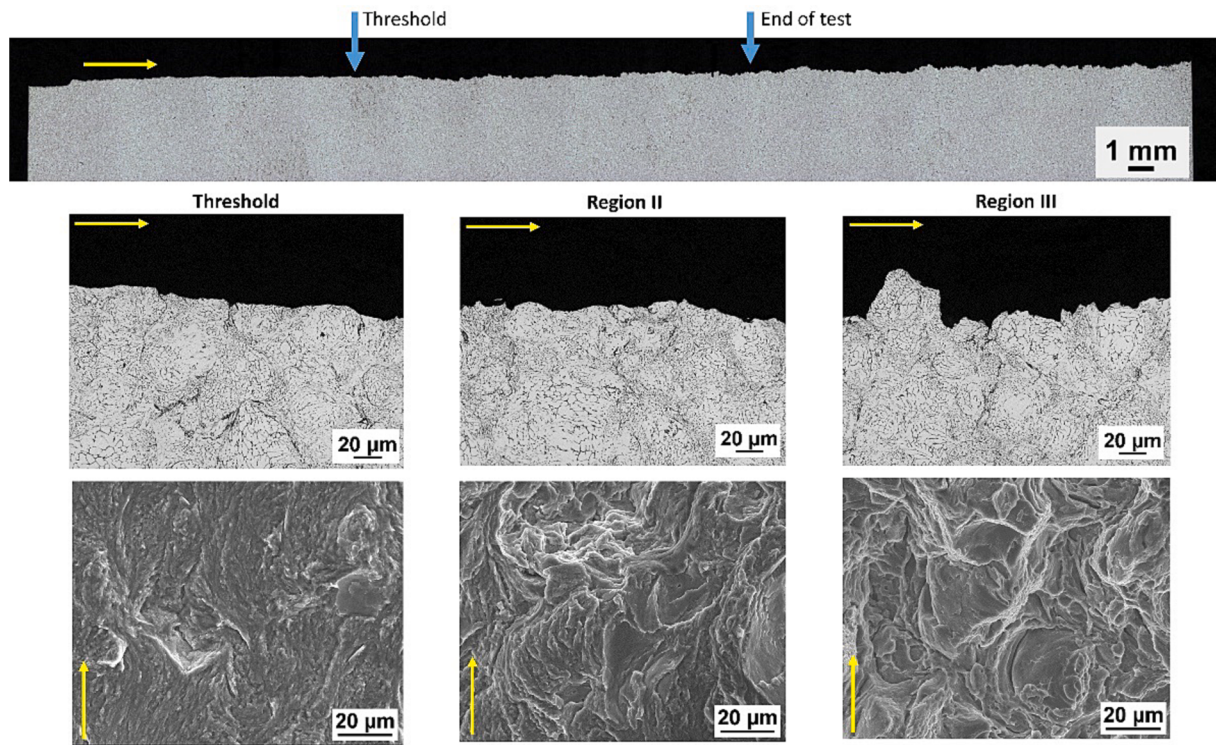


**Fig. 12.** Optical images (panoramic and high-magnification side profiles) and SEM fractography (top view) for as-sprayed CS Al-6061 at  $R = 0.1$  (C(T) specimen, L-T). Yellow arrows indicate crack growth direction.

start of Region III (corresponding to a static plastic zone of  $r_y = 187 \mu\text{m}$ ). The fractographic analysis of CS Al-6061 at  $R = 0.7$ , shown for the two orientations in Figs. 13 and 14, reveals similar mechanisms to the lower stress ratio condition at threshold and in the transition to interparticular growth. However, secondary cracking along particle boundaries is

observed at  $R = 0.7$  that was not present at  $R = 0.1$ .

#### 3.4. Small fatigue crack growth data and mechanisms

Small FCG testing by K-control was conducted on wrought Al-6061-

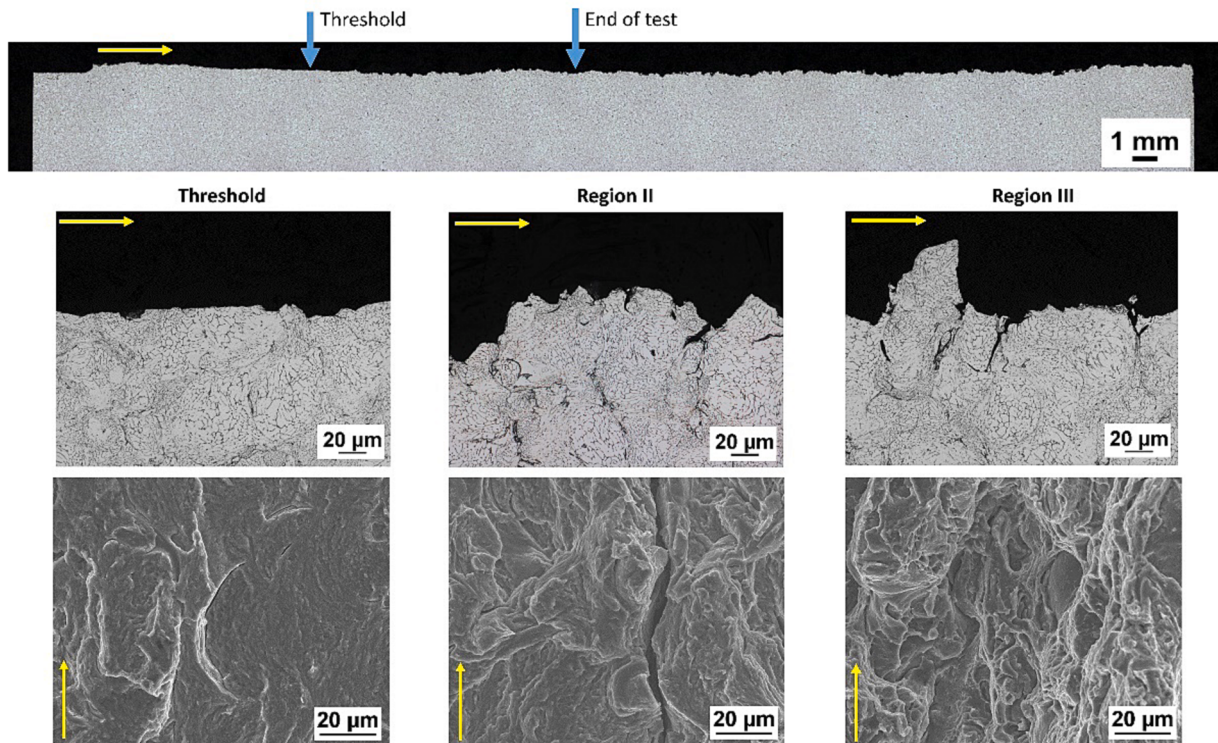


**Fig. 13.** Optical images (panoramic and high-magnification side profiles) and SEM fractography (top view) for as-sprayed CS Al-6061 at  $R = 0.7$  (C(T) specimen, T-L). Yellow arrows indicate crack growth direction.

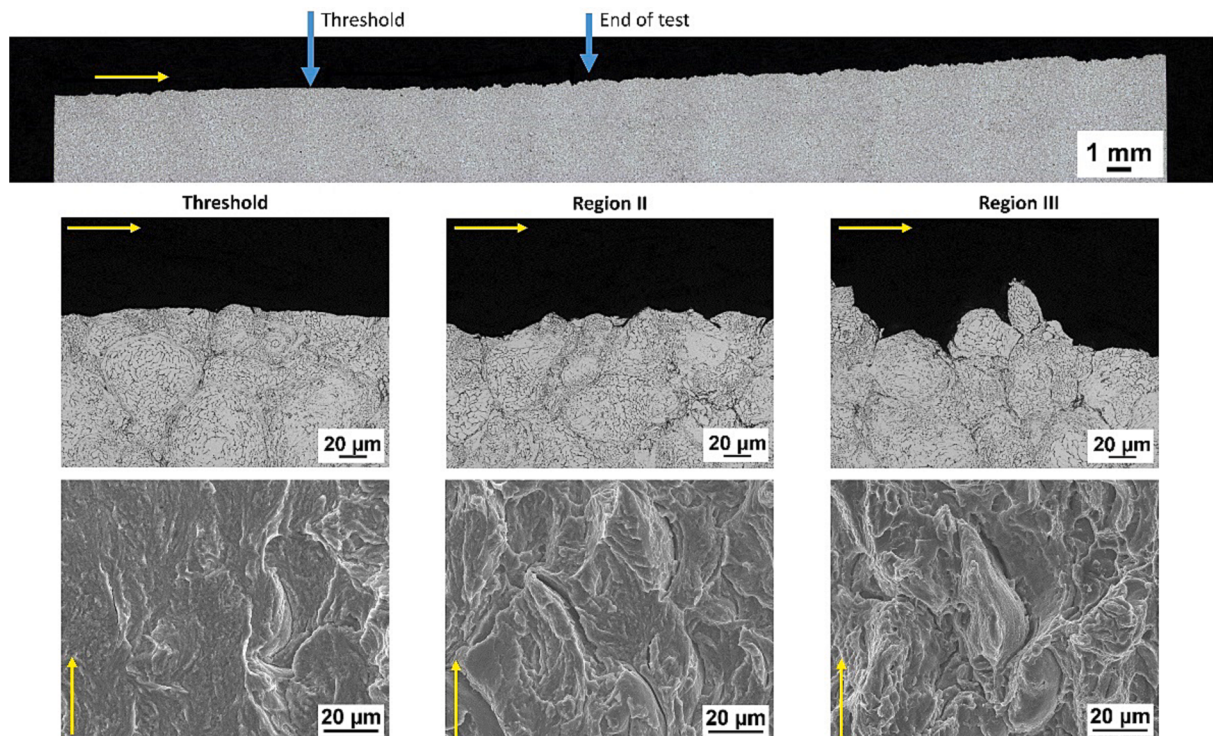


**Fig. 14.** Optical images (panoramic and high-magnification side profiles) and SEM fractography (top view) for as-sprayed CS Al-6061 at  $R = 0.7$  (C(T) specimen, L-T). Yellow arrows indicate crack growth direction.

T6 and as-sprayed bulk CS Al-6061 depositions at  $R = 0.1$ , and the results are summarized in Table 4. Data were collected in K-decreasing mode following pre-cracking from 200  $\mu\text{m}$  notches such that crack sizes at threshold were in the 450–540  $\mu\text{m}$  range. The as-sprayed CS material

had no discernable crack growth rate differences as the crack grew along the T-L and L-T orientations in the plane normal to the deposition direction, Fig. 15(a), because they are grown through the same crack plane. The CS material has a slightly lower small FCG threshold than the

**Table 4**

Summary of FCG thresholds ( $\Delta K_{th-app}$ ) and Paris Law constants (C and m) for all small crack growth testing conditions (processing set III).

Material	Test Specimen	R	Orientation	$\Delta K_{th-app}$ [MPa $\sqrt{m}$ ]	C	m
Wrought Al-6061-T6	SF(T)	0.1	T-L	1.6	$1.1 \cdot 10^{-7}$	2.7
As-sprayed CS Al-6061			T-L	1.4	$5.0 \cdot 10^{-8}$	3.7
As-sprayed CS Al-6061			L-T	1.2	$9.5 \cdot 10^{-8}$	3.1
As-sprayed CS Al-6061			T-S	1.5	$5.0 \cdot 10^{-8}$	3.4
As-sprayed CS Al-6061			L-S	1.3	$4.6 \cdot 10^{-8}$	3.6

wrought material,  $\Delta K_{th-app} = 1.3 \text{ MPa}\sqrt{\text{m}}$  as compared to  $\Delta K_{th-app} = 1.6 \text{ MPa}\sqrt{\text{m}}$ , and the crack growth rates of the two materials match closely in Region I and low Region II. The small FCG curves of the CS material in T-L/L-T orientations both exhibit an inflection point around  $\Delta K_{app} = 7.3 \text{ MPa}\sqrt{\text{m}}$  ( $K_{max} = 8.3 \text{ MPa}\sqrt{\text{m}}$ ) where crack growth accelerates. Optical and SEM fractographic analyses of the small FCG specimens, Fig. 16(a) and Fig. 17, show similar behavior to the long crack growth. At low stress intensities, crack growth is transparticular and insensitive to particle boundaries, and a transition to mixed-mode growth is observed at the same  $\Delta K_{app} = 3.4 \text{ MPa}\sqrt{\text{m}}$ . Crack growth becomes completely

interparticular at  $K_{max} = 8.3 \text{ MPa}\sqrt{\text{m}}$  (T-L) and  $K_{max} = 7.8 \text{ MPa}\sqrt{\text{m}}$  (L-T), which correspond to the inflection point in the FCG curves.

Similar to the T-L and L-T orientations, there are no discernable differences in crack growth rates when the crack grows top-down along the deposition direction (T-S and L-S), Fig. 15(b). Small FCG thresholds closely match the wrought material in Region I and low Region II. Again, the T-S/L-S CS material exhibits an inflection point around  $\Delta K_{app} = 6.5 \text{ MPa}\sqrt{\text{m}}$  ( $K_{max} = 7.2 \text{ MPa}\sqrt{\text{m}}$ ) where crack growth rates increase. Optical and SEM fractographic analyses, Fig. 16(b) and Fig. 18, confirm similar microstructural mechanisms in T-S/L-S orientations to the T-L/L-

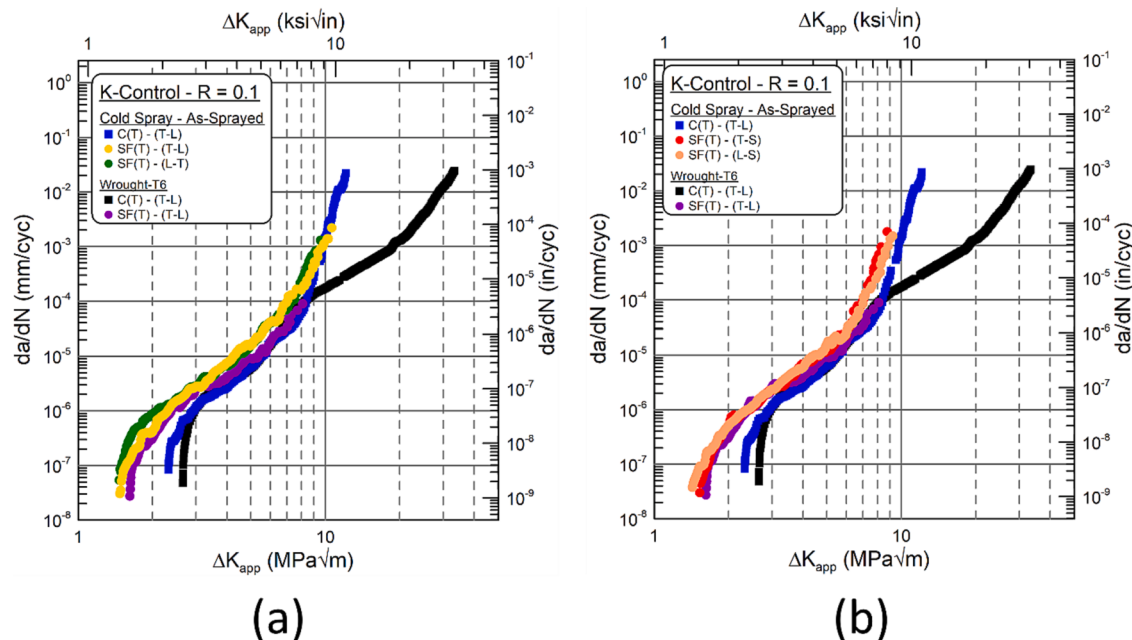


**Fig. 15.** K-control, small FCG curves ( $R = 0.1$ ) for as-sprayed CS Al-6061 in (a) T-L/L-T and (b) T-S/L-S orientations compared with equivalent long FCG data as well as long and small FCG data for wrought Al-6061-T6.

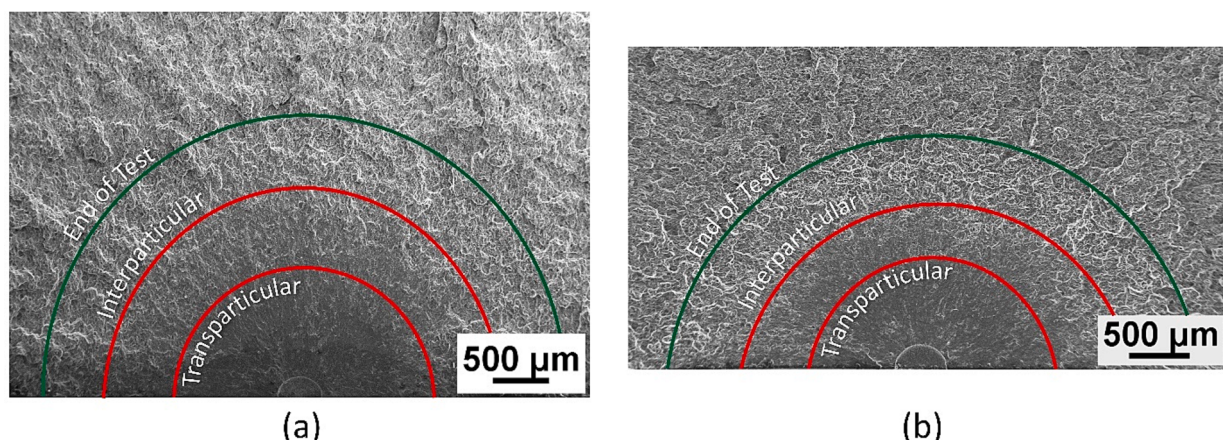


**Fig. 16.** SEM fractographic images showing the transition in crack growth mechanisms for (a) T-L and (b) L-S orientations.

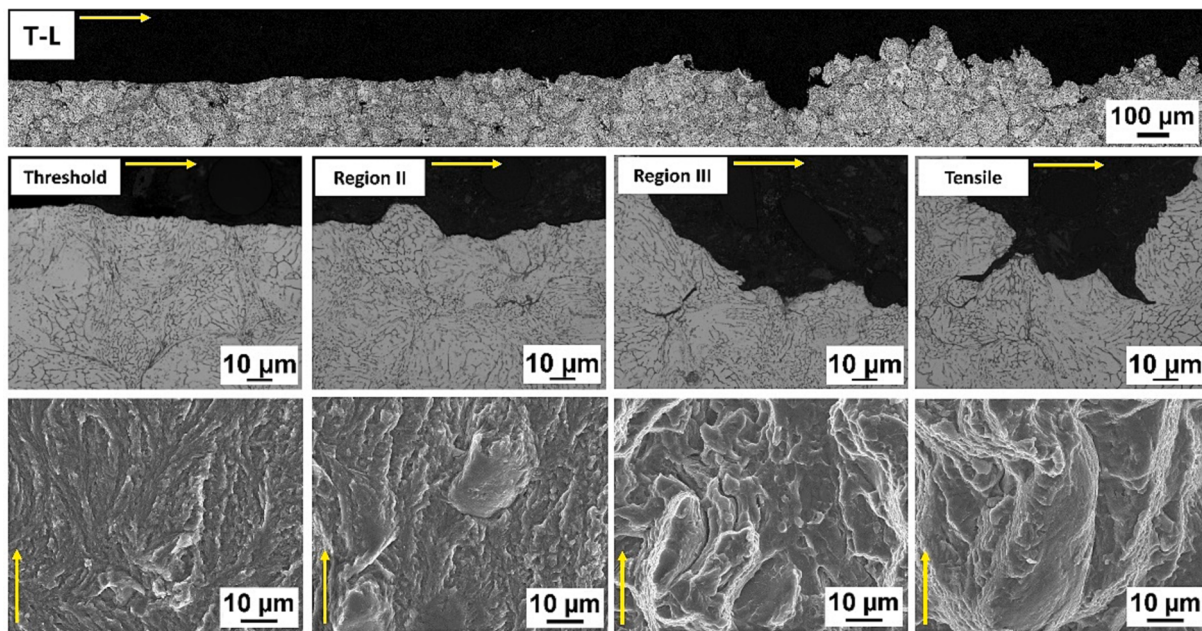


**Fig. 17.** Optical images (panoramic and high-magnification side profiles) and SEM fractography (top view) for as-sprayed CS Al-6061 at  $R = 0.1$  (SF(T) specimen, T-L). Yellow arrows indicate crack growth direction.

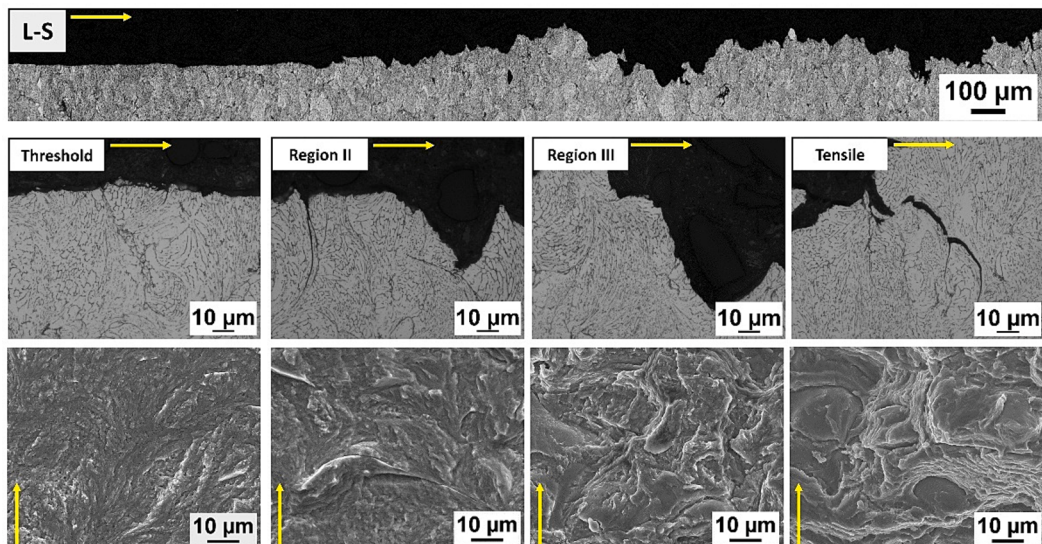


**Fig. 18.** Optical images (panoramic and high-magnification side profiles) and SEM fractography (top view) for as-sprayed CS Al-6061 at  $R = 0.1$  (SF(T) specimen, L-S). Yellow arrows indicate crack growth direction.

T orientations, having a transition from transparticular growth to mixed-mode growth at the same  $\Delta K_{app} = 3.4 \text{ MPa}\sqrt{\text{m}}$  and fully interparticular growth at lower values of  $K_{max} = 7.1 \text{ MPa}\sqrt{\text{m}}$  (T-S) and  $K_{max} = 7.2 \text{ MPa}\sqrt{\text{m}}$  (L-S).

### 3.5. Small crack behavior and closure effects

Further small FCG testing was conducted to clarify the role of crack size at threshold. In the preceding K-control experiments, the crack was grown prior to data collection to produce a naturally sharp tip (and stress concentration) at the expense of having longer crack lengths that diminish the likelihood and magnitude of small crack phenomena. Conversely, load-control experiments collect data from the crack's initiation at the blunt, EDM-machined notch, which may reduce the effective stress concentration and increase the observed crack growth

threshold, but enables data collection at smaller crack sizes. Load-control experiments are also more challenging to conduct due to competition between the machined notch and microstructural features to produce crack initiation, and the experimenter must strike a balance between small notch sizes and the probability of initiation from them. These data are compared in Fig. 19, where the crack lengths of K-control tests at threshold were in the 450–540 µm range and the initial notch size in load-control tests was 200 µm. Notably, no differences in the threshold are observed as a consequence of crack tip shape or length.

The wrought material, having crack sizes of 200 µm and 540 µm at threshold, exhibits microstructurally small FCG phenomena evidenced by the inflection in the load-control test data at  $\Delta K = 1.9 \text{ MPa}\sqrt{\text{m}}$  (no definitive instances are observed in K-control). Fractographic imaging, Fig. 20(a), reveals that growth is predominantly transgranular with an out-of-plane deflection at a crack length corresponding to the

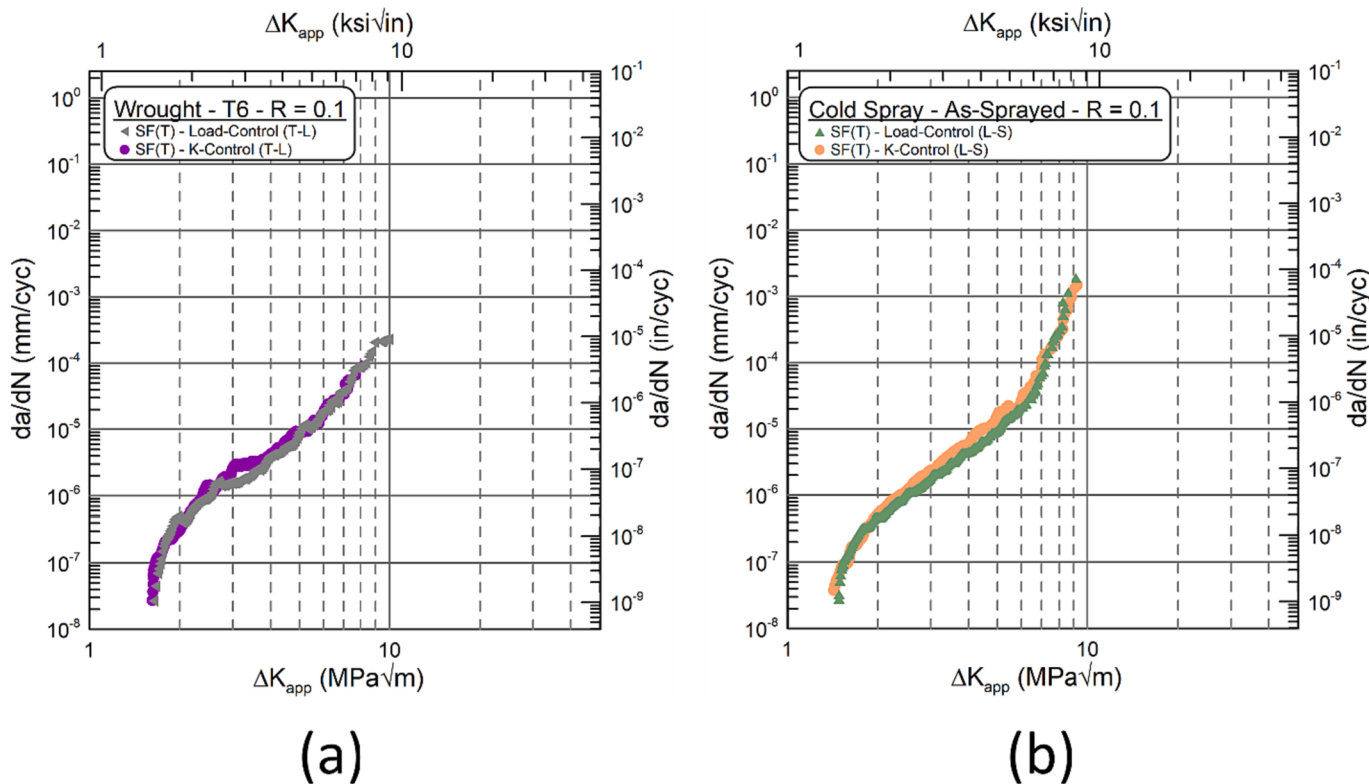


**Fig. 19.** Load-control and K-control small FCG data at  $R = 0.1$  for (a) wrought Al-6061-T6 (T-L orientation) and (b) as-sprayed CS Al-6061 (L-S orientation). The crack sizes at threshold were 200  $\mu\text{m}$  for load-control tests and 40  $\mu\text{m}$  (wrought) and 450  $\mu\text{m}$  (CS) for K-control tests.

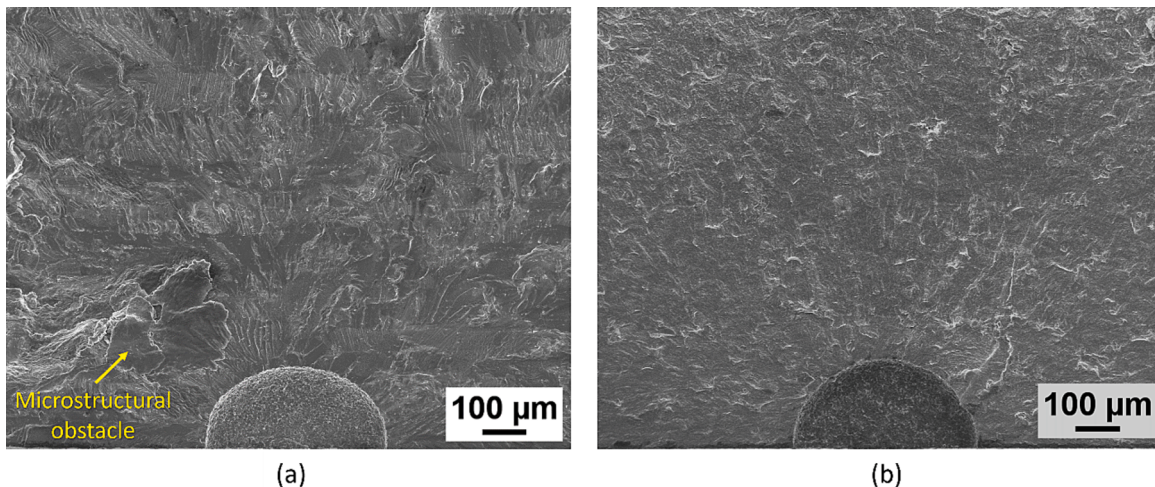


**Fig. 20.** SEM fractography of small FCG (load-control tests) showing the initial notch and growth at threshold for (a) wrought Al-6061-T6 and (b) as-sprayed CS Al-6061.

deceleration event. This feature may represent the crack's arrest at a grain boundary or crack tip bifurcation, however further study would be required to confirm the cause of crack deceleration. No such interactions are observed for the CS material in either the FCG data or fractographic studies. Crack growth was transparticular throughout the threshold, and no powder particle boundaries were observed on the fracture surfaces, Fig. 20(b).

These results are not unexpected, considering that small crack phenomena typically occur up to crack lengths 5–10 times the microstructural feature size. The wrought material, having a grain size of 59  $\mu\text{m}$  in the direction of crack growth, is below this limit from its initiation and therefore can sample a large volume of material for obstacles before

outgrowing the small crack regime. Conversely, the CS material has a particle size of 35  $\mu\text{m}$ , which gives heuristic small crack size limits of 175 – 350  $\mu\text{m}$ . Small crack growth phenomena, if present in the CS material, are then less likely to be observed at a 200  $\mu\text{m}$  notch size, either because the small crack size limit has been exceeded or there is less volume of material in which to sample such a microstructural feature. However, these results do not preclude the presence of small crack behavior in CS materials. Intrinsic microstructural defects smaller than the notch size are likely to exist, considering that powder particles approximately 100  $\mu\text{m}$  in diameter are observable on fracture surfaces and crack initiation from the 200  $\mu\text{m}$  notch was reliable (i.e., intrinsic defects are likely to exist in the 100 – 200  $\mu\text{m}$  range). Furthermore, anisotropy of powder

particle boundary orientations, being more likely to orient perpendicular to the deposition direction, may change the likelihood of crack interactions in other crack plane orientations.

To further assess the effect of crack size on threshold behavior, the ACR crack closure correction was applied to the long FCG data to calculate effective, physically small threshold values,  $\Delta K_{\text{th-eff}}$ . The wrought Al-6061-T6 had  $\Delta K_{\text{th-eff}} = 1.9 \text{ MPa}\sqrt{\text{m}}$ , as compared to the applied value of  $\Delta K_{\text{th-app}} = 2.6 \text{ MPa}\sqrt{\text{m}}$ , Fig. 21(a). The small FCG threshold is further lower than both of these values due to small crack size effects that are distinct from closure effects. The CS Al-6061 had  $\Delta K_{\text{th-eff}} = 1.1 \text{ MPa}\sqrt{\text{m}}$  (T-L) and  $\Delta K_{\text{th-eff}} = 1.3 \text{ MPa}\sqrt{\text{m}}$  (L-T) after ACR corrections, as compared to the applied values of  $\Delta K_{\text{th-app}} = 2.3 \text{ MPa}\sqrt{\text{m}}$  (T-L) and  $\Delta K_{\text{th-app}} = 2.2 \text{ MPa}\sqrt{\text{m}}$  (L-T), Fig. 21(b). The crack growth thresholds measured with SF(T) specimens are higher than the closure-corrected thresholds for both crack orientations,  $\Delta K_{\text{th-app}} = 1.4 \text{ MPa}\sqrt{\text{m}}$  (T-L) and  $\Delta K_{\text{th-app}} = 1.2 \text{ MPa}\sqrt{\text{m}}$  (L-T). Given that these values are similar to the estimated physically small crack thresholds, these data indicate that the cracks in CS Al-6061 may be affected by closure even at 200  $\mu\text{m}$  in length, and are physically small, not microstructurally small.

### 3.6. Interfacial strength evaluation using lap shear testing

Limited by the height of the deposition and the inability to extract specimens, long crack growth testing along the S-T and S-L directions could not be conducted. Lap shear testing was alternatively used to evaluate the interface shear strength between the CS deposition and substrate. Lap shear testing was conducted for specimens with varied ductility from processing sets I and II, and the results are shown in Fig. 22. The greater shear strength of the coating in processing set II is attributed to the improved powder handling, which is believed to reduce the number and/or severity of particle boundary defects. This is supported by observation of the fracture surface of the higher ductility coating, Fig. 23, revealing combined dimpling along particle boundaries and transparticular fracture, indicating effective particle bonding.

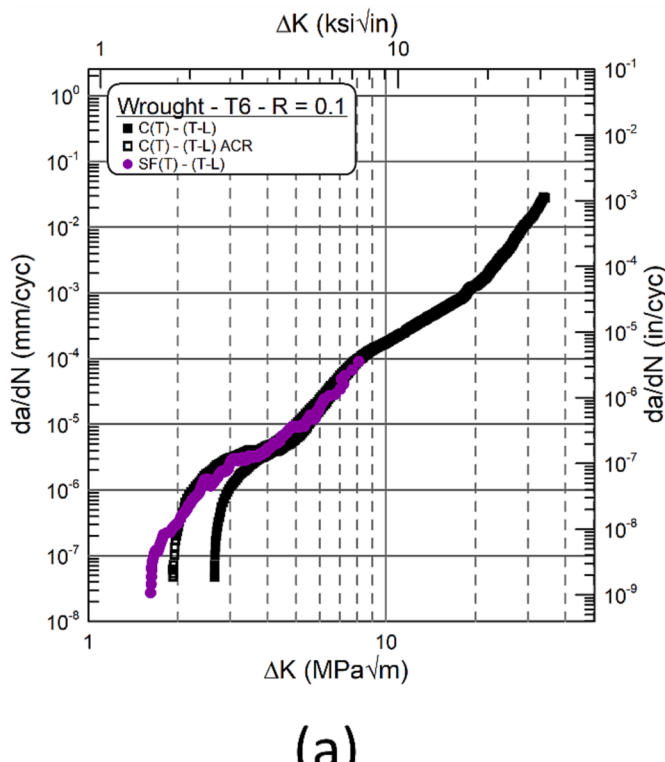


Fig. 21. Test data from long crack and K-control small crack growth testing at  $R = 0.1$ , along with ACR-corrected long FCG data, for (a) wrought Al-6061-T6 and (b) as-sprayed CS Al-6061 (T-L and L-T orientations).

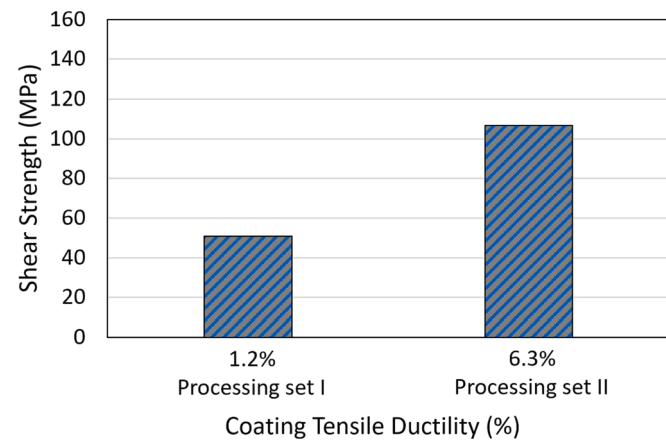
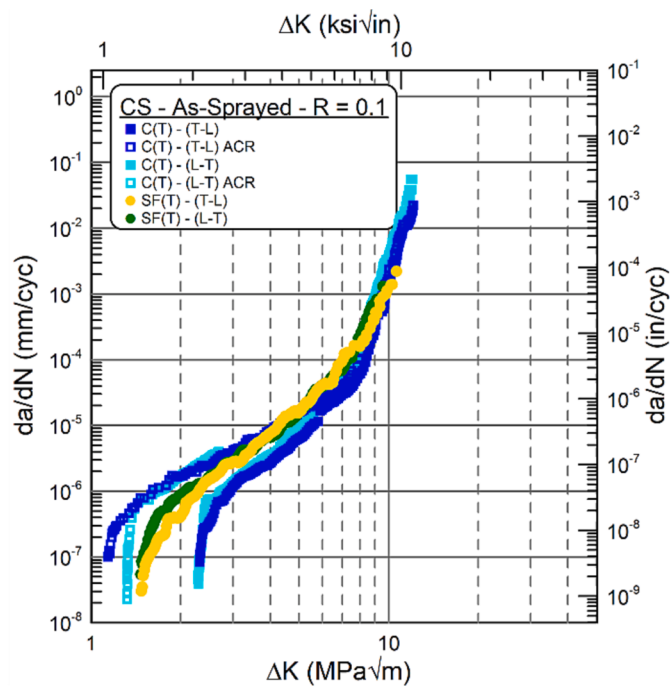


Fig. 22. Lap shear test results for CS Al-6061 depositions with different ductility on wrought Al-6061-T6 substrates. Note that ASTM D1002, on which this test method is based, is intended for comparative purposes only, and measured strengths should not be used to specify design-allowable stress values.

### 3.7. Onset of interparticular crack growth

Long FCG testing indicates that interparticular growth in Regions II and III is detrimental to the crack growth resistance of as-sprayed CS Al-6061 by limiting its fracture toughness. These crack growth mechanisms are closely related to ductility, which allows for greater amounts of crack extension before failure. Fig. 24 shows the ductility of each deposition plotted against the strain energy release rate,  $G$ , calculated with  $K_I = K_{\max}$  at the onset of interparticular crack growth using Eqn. (1) (and  $K_{II} = 0$ ). These data include as-sprayed and annealed conditions, varied stress ratio (0.1 to 0.7) and test type (long and small crack), and also integrate data collected by Gavras et al. [18]. Strain energy release



(b)

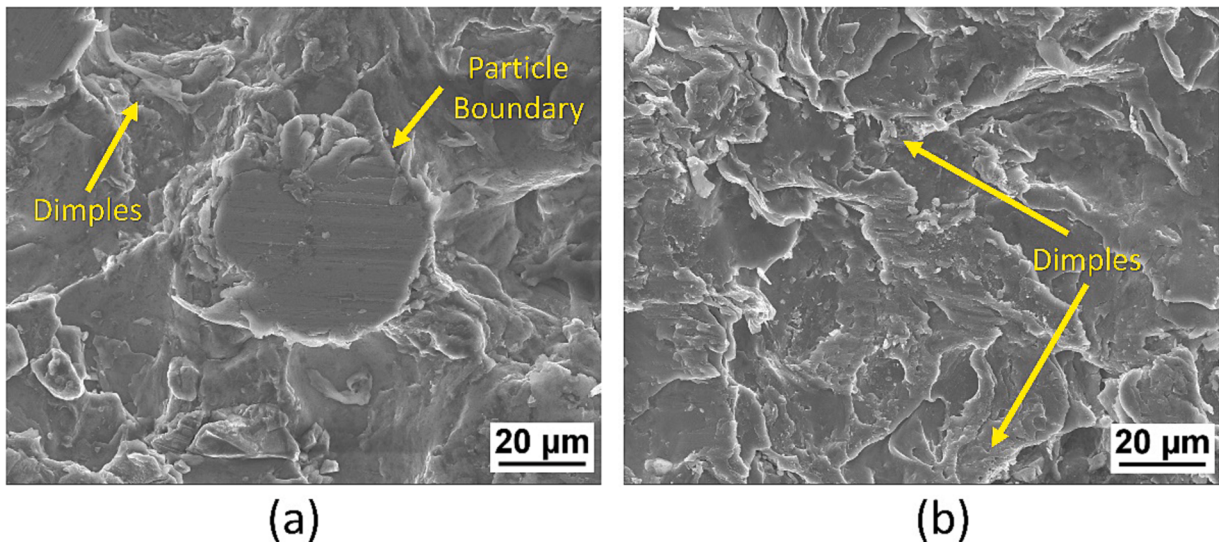


**Fig. 23.** Fracture surfaces produced by the lap shear test of the interface between CS Al-6061 deposition and wrought Al-6061-T6 substrate from processing set II on (a) the CS side and (b) the wrought side of the fractured specimen.

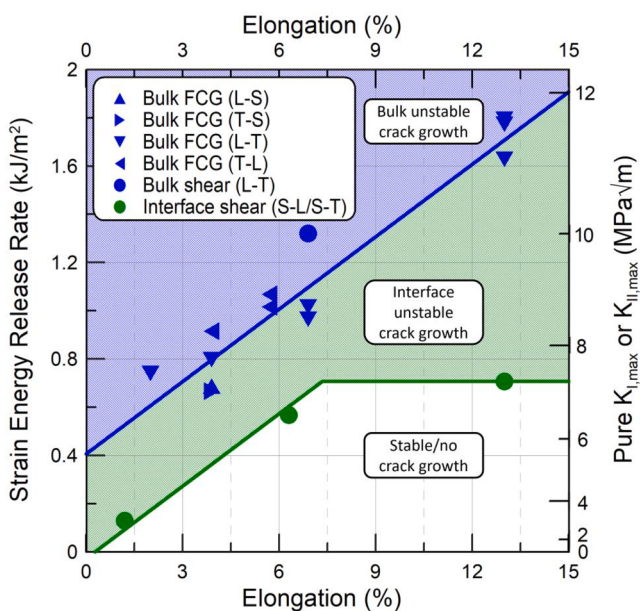


**Fig. 24.** Design map indicating the transition between stable crack growth and interparticle failure for the T-S and L-S planes in bulk CS Al-6061 (upper line) and the L-T plane along the CS-substrate interface (lower line; as-sprayed Al-6061 on wrought Al-6061-T6). Directions in parentheses denote the orientations specified for crack growth and shear testing. For shear tests, note that shear strengths measured using ASTM D1002 are not intended to be used to specify design-allowable stress values, and their derivative strain energy release rates and stress intensity factors carry the same limitations. Data for bulk FCG at 2 and 13 percent elongation were taken from literature [18,31].

rate was selected because it can be compared across varied loading modes, thus allowing comparison between the FCG data in the T-S and L-S planes with  $G$  values calculated for the L-T plane from shear testing data. This was done using stress intensity factor solutions for lap shear testing of welds, given by Eqns. (2) and (3) [30]. In these equations,  $F$  is the peak force experienced during testing,  $W$  is the width of the interface,  $t$  and  $b$  are the thickness and width of the fixture,  $K_I$  and  $K_{II}$  are the mode I and II maximum stress intensity factors, and  $\nu$  and  $E$  are the Poisson's ratio and elastic modulus of Al-6061, respectively. The resulting fracture mechanics properties are  $K_I = 0.9 \text{ MPa}\sqrt{\text{m}}$ ,  $K_{II} = 3.0$

$\text{MPa}\sqrt{\text{m}}$ , and  $G = 130 \text{ J/m}^2$  for the low ductility coating (processing set I) and  $K_I = 1.8 \text{ MPa}\sqrt{\text{m}}$ ,  $K_{II} = 6.3 \text{ MPa}\sqrt{\text{m}}$ , and  $G = 570 \text{ J/m}^2$  for the high ductility coating (processing set II). Other strain energy release rate values were taken from the authors' other shear testing studies [31].

$$G = \frac{1 - \nu^2}{E} (K_I^2 + K_{II}^2) \quad (1)$$

$$K_I = \frac{\sqrt{3}}{2} \frac{F}{b\sqrt{t}} \frac{W}{2t} \quad (2)$$

$$K_{II} = 1.0285 \left( \frac{W}{t} \right)^{-0.242} \frac{F}{b\sqrt{t}} \quad (3)$$

The lines on the map delineate the transitions between stable crack growth and interparticle failure for the T-S and L-S planes in bulk CS deposits (upper line) and the L-T plane along the CS-substrate interface (lower line). The upper transition line is calculated from all FCG data (triangles) and has  $R^2 = 0.937$ , indicating that tensile ductility is a good predictor for the onset of unstable interparticle FCG independent of heat treatment and stress ratio. Comparison with the strain energy release rate converted from shear testing of the L-T plane (circle) indicates good agreement with FCG data, supporting the use of Eqns. 1–3 to calculate  $G$  from shear testing, although it may be slightly non-conservative. The lower transition for interface failure consists of two line segments, one parallel to the upper transition and corresponding to the similar ductility sensitivity as the FCG data, and the other at a fixed value,  $G = 710 \text{ J/m}^2$ , due to the deviation from linearity by the point at 13 percent elongation. Additionally, although the shear tests produce mixed-mode loading, it is possible to use Eqn. (1) to calculate a pure mode I or mode II stress intensity factor. These values are shown on the second ordinate axis and predict an upper limit to crack growth along the interface of  $K_{I,\max} = K_{II,\max} = 7.3 \text{ MPa}\sqrt{\text{m}}$ .

Microstructure is thought to play a significant role in the offset of the two transition lines and the non-linear variation of  $G$  with ductility for the interface. Fig. 25 indicates the orientation of the crack relative to particle and substrate interfaces, where bulk testing samples orient the crack out of the deposition plane (less particle interface area) and interface shear testing places the crack within the deposition plane (more particle interface area). As seen from fractographic observations, defects generally occur in the deposition (L-T) plane due to poor adhesion on impact. Therefore, cracks grown in the L-S and T-S planes (T-L, T-S, L-S, and L-T orientations) are less likely to interact with these

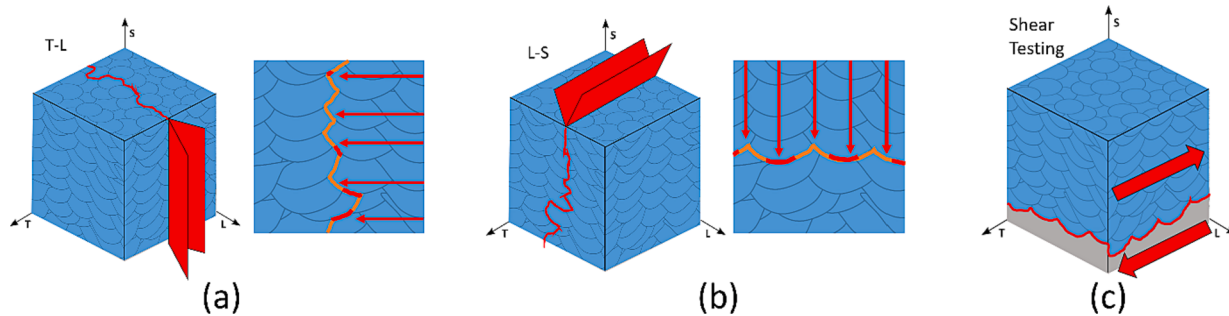


**Fig. 25.** (a,b) FCG mechanisms of CS Al-6061 for interparticular growth in the T-L (or L-T) and L-S (or T-S) orientations, and (c) the coating-substrate interface under shear loading in S-L or S-T orientations.

defects and exhibit greater toughness values than in the L-T plane (S-L and S-T orientations). Additional differences in the strength of the interface may also be attributed to phenomena that only occur at the CS-substrate interface, such as entrapped polishing media, oxides and defects on the substrate surface, and transient thermal phenomena at the start of the deposition process. The interface was also proposed to have a bilinear toughness variation with ductility, suggesting that there is an upper bound to increases in crack growth resistance of the CS-substrate interface with greater ductility. It is noteworthy that the specimen at 13 percent elongation was annealed, whereas the other two interfaces are as-sprayed, which may indicate that annealing does not substantially improve interface toughness, although further testing is necessary to support these observations. This is plausible, however, if the interfacial defects occur due to entrapped surface contaminants or large voids that are not healed by diffusion during annealing in the same way as bulk defects.

#### 4. Conclusions

The goal of this study is to expand the understanding of crack growth behavior in CS Al-6061 depositions to support design for high-integrity structural applications. A summary of the important findings and developments from this study are presented here.

- Tensile properties of CS depositions are influenced by processing parameters and powder storage/handling. The two higher ductility CS conditions (3.9 and 6.9 percent elongation) had ultimate tensile strengths of approximately 290 MPa, 8.5 % lower than the wrought Al-6061-T6 material. Yield strength varied between the three processing sets and had an inverse relationship with the ductility; the higher the ductility, the lower the yield strength.
- Long FCG studies indicate that CS Al-6061 has a slightly lower long crack growth threshold than wrought Al-6061-T6. Crack growth rates are similar to the wrought material in Region II and then increase at the start of Region III due to the transition to completely interparticular growth. The onset of interparticular growth was observed to occur in the range  $K_{\max} = 8.5 - 9.0 \text{ MPa}\sqrt{\text{m}}$  for various crack-deposition orientations.
- Small FCG studies were conducted, however crack sizes of 200  $\mu\text{m}$  and larger did not exhibit microstructurally small crack effects, and the cracks were instead deemed physically small. Thresholds of physically small cracks are similar to wrought Al-6061-T6 due to the fine microstructure and limited closure. The onset of interparticular growth was measured to occur in the range  $K_{\max} = 7.1 - 8.3 \text{ MPa}\sqrt{\text{m}}$  for various crack-deposition orientations.
- Design maps were created to relate tensile ductility of CS depositions to crack growth stability at prescribed loading conditions. The strain energy release rate at the onset of interparticular crack growth in bulk CS follows a linear relationship with ductility. A method to predict this behavior using shear test data was proposed and used to

extend the stability map to the CS-substrate interface. This approach can further be used to predict mixed-mode stress intensity factors for stable crack growth, and a limiting mode I fracture toughness of the CS-substrate interface of  $K_{\max} = 7.3 \text{ MPa}\sqrt{\text{m}}$  was determined.

#### CRediT authorship contribution statement

**Christopher M. Sample:** Formal analysis, Investigation, Methodology, Visualization, Writing – original draft, Writing – review & editing. **Anthony G. Spangenberger:** . **Victor K. Champagne:** Funding acquisition, Project administration, Resources, Writing – review & editing. **Diana A. Lados:** Funding acquisition, Project administration, Supervision, Writing – review & editing.

#### Declaration of competing interest

The authors declare that they have no known competing financial interests or personal relationships that could have appeared to influence the work reported in this paper.

#### Data availability

The data that has been used is confidential.

#### Acknowledgements

This research was funded through the Army Research Laboratory, Cooperative Research Agreement W911NF-15-2-0024 and the Integrative Materials Design Center (iMdc) at Worcester Polytechnic Institute (WPI). A special thank you is extended to the iMdc members for their insight and technical support.

#### References

- [1] V.K. Champagne, The cold spray materials deposition process, Woodhead Publishing, 2007, pg.1.
- [2] Champagne VK, Ozdemir OC, Nardi A. *Practical cold spray*. Springer 2021:1–3.
- [3] Dykhuizen RC, Smith MF, Gilmore DL, Neiser RA, Jiang X, Sampath S. Impact of high velocity cold spray particles. *J Therm Spray Technol* 1999;8(4):559–64. <https://doi.org/10.1361/105996399770350250>.
- [4] Moridi A, Hassani-Gangaraj SM, Vezzù S, Trško L, Guagliano M. Fatigue behavior of cold spray coatings: The effect of conventional and severe shot peening as pre-/post-treatment. *Surf Coat Technol* 2015;283:247–54. <https://doi.org/10.1016/j.surfcoat.2015.10.063>.
- [5] Sample CM, Champagne VK, Nardi AT, Lados DA. Factors governing static properties and fatigue, fatigue crack growth, and fracture mechanisms in cold spray alloys and coatings/repairs: A review. *Addit Manuf* 2020;36:101371.
- [6] Cavaliere P, Silvello A. Fatigue behaviour of cold sprayed metals and alloys: critical review. *Surf Eng* 2016;32(9):631–40. <https://doi.org/10.1179/1743294415Y.0000000100>.
- [7] Moridi A, Hassani-Gangaraj SM, Guagliano M, Dao M. Cold spray coating: review of material systems and future perspectives. *Surf Eng* 2014;30(6):369–95. <https://doi.org/10.1179/1743294414Y.0000000270>.
- [8] White BC, Story WA, Brewer LN, Jordon JB. Fatigue behavior of freestanding AA2024 and AA7075 cold spray deposits. *Int J Fatigue* 2018;112:355–60. <https://doi.org/10.1016/j.ijfatigue.2018.03.007>.

- [9] Yamazaki Y, Fukanuma H, Ohno N. Anisotropic Mechanical Properties of the Free-standing Cold Sprayed SUS316 Coating and the Effect of the Post-spray Heat Treatment on it. *J Jpn Therm Spraying Soc* 2016;53(3):91–5. <https://doi.org/10.11330/jtss.53.91>.
- [10] Al-Mangour B, Dallala R, Zhim F, Mongrain R, Yue S. Fatigue behavior of annealed cold-sprayed 316L stainless steel coating for biomedical applications. *Mater Lett* 2013;91:352–5. <https://doi.org/10.1016/j.matlet.2012.10.030>.
- [11] Bagherifard S, Monti S, Zuccoli MV, Riccio M, Kondás J, Guagliano M. Cold spray deposition for additive manufacturing of freeform structural components compared to selective laser melting. *Mater Sci Eng, Proc Conf* 2018;721:339–50. <https://doi.org/10.1016/j.mseia.2018.02.094>.
- [12] ASTM International. E647-15e1 Standard Test Method for Measurement of Fatigue. Crack Growth Rates 2015.
- [13] Lados DA, Apelian D, Donald JK. Fatigue crack growth mechanisms at the microstructure scale in Al-Si-Mg cast alloys: Mechanisms in the near-threshold regime. *Acta Mater* 2006;54(6):1475–86.
- [14] Ritchie R, Lankford J. Small fatigue cracks: a statement of the problem and potential solutions. *Mater Sci Eng* 1986;84:11–6.
- [15] Suresh S, Ritchie R. Propagation of short fatigue cracks. *International Metals Reviews* 1984;29(1):445–75.
- [16] Cavaliere P, Perrone A, Silvello A. Fatigue behaviour of Inconel 625 cold spray coatings. *Surf Eng* 2018;34(5):380–91. <https://doi.org/10.1080/02670844.2017.1371872>.
- [17] Kovarik O, Siegl J, Cizek J, Chraska T, Kondás J. Fracture Toughness of Cold Sprayed Pure Metals. *J Therm Spray Technol* 2020;29(1):147–57. <https://doi.org/10.1007/s11666-019-00956-z>.
- [18] Gavras AG, Lados DA, Champagne VK, Warren RJ. Effects of processing on microstructure evolution and fatigue crack growth mechanisms in cold-spray 6061 aluminum alloy. *Int J Fatigue* 2018;110:49–62. <https://doi.org/10.1016/j.jfatigue.2018.01.006>.
- [19] A.G. Gavras, D.A. Lados, V. Champagne, R.J. Warren, D. Singh, Small Fatigue Crack Growth Mechanisms and Interfacial Stability in Cold-Spray 6061 Aluminum Alloys and Coatings, 49(12) (2018) 6509-6520. <https://doi.org/10.1007/s11661-018-4929-0>.
- [20] Julien SE, Nourian-Aval A, Liang W, Schwartz T, Ozdemir OC, Müftü S. Bulk fracture anisotropy in Cold-Sprayed Al 6061 deposits. *Eng Fract Mech* 2022;263:108301.
- [21] ASTM International, E8/E8M-16a Standard Test Methods for Tension Testing of Metallic Materials, 2016.
- [22] Donald JK. Introducing the compliance ratio concept for determining effective stress intensity. *Int J Fatigue* 1997;19(93):191–5.
- [23] J.K. Donald, A. Blair. Automated fatigue crack growth testing and analysis manual, Version 3+.15.12, Users' steady state reference manual. Bethlehem, PA, USA, Fracture Technology Associates, 2015. Available online at: <https://fracturetech.com/download/9/manuals/1047/fcgr-testing-and-analysis-manual.pdf>.
- [24] ASTM International, ASTM D1002 – 10 Standard test method for apparent shear strength of single-lap-joint adhesively bonded metal specimens by tension loading (metal-to metal), 2016.
- [25] MIL-J-24445A Department of Defense Military Specification, March 1, 1971.
- [26] ASTM International, E112-13 Standard Test Methods for Determining Average Grain Size, 2021.
- [27] Sabard A, Hussain T. Inter-particle bonding in cold spray deposition of a gas-atomised and a solution heat-treated Al 6061 powder. *J Mater Sci* 2019;54(18):12061–78.
- [28] Rokni M, Widener C, Champagne V. Microstructural evolution of 6061 aluminum gas-atomized powder and high-pressure cold-sprayed deposition. *J Therm Spray Technol* 2014;23(3):514–24.
- [29] Champagne VK. Investigation of the effect of oxides on the critical impact velocity during the cold spray process of high purity aluminum powder. PhD thesis, Worcester Polytechnic Institute December 2018;13:133. <https://digital.wpi.edu/etd/nc580m852>.
- [30] Sripathi K, Asim K, Pan J. Stress intensity factor solutions for estimation of fatigue lives of laser welds in lap-shear specimens. *Eng Fract Mech* 2011;78(7):1424–40.
- [31] Sample CM, Spangenberger AG, Champagne VK, Lados DA. Fatigue Crack Growth Mechanisms and Methods to Evaluate the Interfacial Strength of Cold Spray Al-6061 Depositions on Similar Al-6061-T6 and Dissimilar Mg-AZ91E-T6 Substrates for Coatings/Repairs, internal report. Integrative Materials Design Center 2022.